Accuracy of Numerical and Analytical Models for Nonlinear Pendulum Motion

Aarav Srivastava

Abstract:

This paper studies the accuracy of various theoretical models of pendulum oscillatory motion by comparing them to experimentally determined data. Pendulums, though often simplified in introductory physics, display nonlinear behavior at large amplitudes, along with significant damping effects. To explore this, equations of motion for the small-angle approximated, drag-free and drag-induced model were solved numerically in Python, and compared to experimental data. Results showed the increasing unreliability of the small-angle approximated and drag-free model with larger amplitudes. At these angles of release, only the drag-induced model sufficiently captures amplitude and period decay, though its accuracy depends strongly on damping coefficient setup.

INTRODUCTION

Background

Galileo Galilei systematically studies the oscillatory motion of a pendulum and proposes its isochronism – the notion that the period of swinging motion remains nearly constant for small amplitudes or initial displacements. This idea remains greatly influential in the field of timekeeping and led to, in 1656, Christiaan Huygens developing the first clock working on the basis of pendulums [1]. Isaac Newton later analyzes pendulums in his *Principia Mathematica*, confirming that their nature could be modeled definitively through deterministic laws of motion, and the period of swing depends solely on the pendulum's length, not its mass [2].

Beyond its historical relevance, the pendulum remains a crucial tool in scientific modelling. A linear approximation is utilized to model pendulums in preliminary study, but this idea breaks down when predicting real-world systems that follow analytically unsolvable governing equations. Understanding the transition from the simplified, linear regime to the real-world nonlinear domain is foundational in modeling pendulum systems.

Pendulum dynamics lie at the core of many physical and engineering situations and systems. The nonlinear pendulum provides crucial insight into oscillatory behavior far beyond the scope of mechanics. Its mathematical setup recurs across fields ranging from electrical engineering, seismology and structural mechanics. The pendulum is among the most widely studied systems in physics and control theory [3]. Thus, understanding the nonlinear behavior of any type of pendulum is not simply academic but foundational for real-world modeling and design.

Simplified idealized pendulum models, especially those assuming small angles, no damping, and massless strings, are often taught in introductory physics. However, they fail when applied to real contexts and systems. For instance, the commonly applied small-angle approximation $\sin\theta \approx \theta$ brings to rise relevant error beyond initial angular displacements of about 20°, causing the predicted period to underestimate the actual time taken for a full oscillation [4]. At 45°, the deviation is already more than 4% [5]. Moreover,

other contributing factors such as friction at the pivot and air resistance introduce energy loss, leading to damped motion that cannot be captured accurately by ideal equations. In real systems, however, this damping is important to model as it influences stability and longevity of oscillations which are properties crucial to consider in engineering design [6].

Expanding on the contexts of pendulums, its relevance extends far beyond mechanical systems. Its mathematical formulation appears in various fields that are denoted by second-order differential equations with sinusoidal or restoring forces.

In electrical engineering, RLC circuits composed of resistors, inductors and capacitors follow equations that are formally identical to damped harmonic oscillators. The voltage across an inductor, for example, in such circuits obeys a differential equation analogous to a pendulum with friction [7]. In more complicated systems like superconducting Josephson junctions, the current-phase relationship is modeled by the nonlinear differential equation $\ddot{\phi}+\sin\phi=0$, which is fundamentally identical to the undriven nonlinear pendulum [8].

In mechanical and civil engineering, structures such as buildings, bridges and towers experience oscillatory behavior under wind or seismic forces. Tall skyscrapers act as inverted pendula, with their top floors swaying in response to external perturbations. Engineers attempt to mitigate this using tuned mass dampers – large, suspended masses that function exactly like pendulums to absorb vibrational energy. The Taipei 101 skyscraper, for example, makes use of a 728-ton heavy pendulum damper that reduces swaying by up to 40% [9]. Bridges use similar mass-spring-damper systems to prevent resonant oscillations in decks and cables.

In seismologic applications, traditional seismometers are based on pendulum-like mechanisms. These instruments detect ground motion by measuring relative displacement between a swinging mass and the Earth's movement. The sensitivity and response of these systems depend largely on pendulum dynamics [10].

These examples show that pendulum-like equations form a unifying mathematical structure in science and engineering. The study of their nonlinear dynamics thus contributes directly to understanding and optimizing real-world systems.

Some physical models bring about equations with no simple closed-form solution. For example, the true motion of a pendulum involves the nonlinear term of sinθ and leads to elliptic integrals rather than the elementary functions involved in analytical solutions. When additional factors of friction, air resistance – forms of damping in pendulums – and external driving forces are involved, the system can become analytically intractable [12]. In such cases, such as large-angle swings of the pendulum or the chaotic double pendulum, computer simulation must be turned to study its swinging behavior. Numerical simulation uses computers to integrate the equations step by step when exact formulas are inapplicable [13].

An analytical solution of a differential equation is an exact formula or expression that agrees to the equation for all time and all input values. On the other hand, a numerical solution computes approximate values at discrete selected points [14]. Analytical solutions are preferred when possible because they are exact ones. However, when the equations are too complicated, the only option is to generate a sequence of numerical approximations through solving step by step.

In cases such as the pendulum where equations are no longer simple, analytical methods tend to break down. They work well for linear problems with constant coefficients but fail when nonlinear terms appear. Likewise, adding damping (which is velocity-dependent) or periodic forcing makes closed-form solutions impossible except in special approximations. Multi-body problems also defeat analytic formulas; for instance, the three-body gravitational problem has no general solutions. Even the damped, driven pendulum only gives a known solution in the small-angle limit; for large oscillations, it has the ability to exhibit chaotic behavior [12].

A numerical simulation is the process of using algorithms and computers to approximate the behavior of a physical system by solving its mathematical model step by step. In practice, one sets up differential equations that govern the system and then uses a computer to calculate the adapting solution at multiple time points. Numerical simulation is indispensable for complex physical problems, as it allows virtual experiments and design before building real prototypes [13].

Utilizing simulation, building dynamic models of pendulums is possible. These techniques are used to simulate the pendulum's motion under various forces, enabling the exploration of its behavior beyond what analytic formulas can show.

Dynamic modeling involves transforming a real physical system into a set of mathematical equations that predict its behavior over time. In practice, fundamental principles such as Newton's Laws or energy conservation are used to derive equations of motion for the system [16]. For a pendulum, this means relating gravitational torque and inertia to obtain differential equations for the angle and angular velocity. In general, a dynamic model of a pendulum becomes a set of ordinary differential equations (ODEs) that completely describe how the state variables involved in the motion change with respect to time [16].

To make the pendulum model tractable, certain idealizations are assumed. Common assumptions include treating the bob as a point mass and the support as a rigid, massless rod or string. One also typically assumes a frictionless pivot and no air resistance – when damping is not considered [17]. Including a damping term to the equation proportional to velocity produces decaying amplitudes and slightly longer periods. A damped pendulum has a longer period, with amplitude shrinking over time [18].This means that a real pendulum takes longer to swing, and their amplitude shrinks over time.

A simulation is a computational process that solves the model's equation over a time span. A numerical solver can handle even very complicated or coupled equations that have no analytic solution. The trade-off is that the solution is only approximate with its accuracy depending on the selected method, the time step size and the error control [16].

Dynamic simulation offers capabilities beyond manual calculation. Once the equations are implemented, the computer can model behavior for any chosen initial angle or length and instantly show how motion varies. In chaotic systems, small changes in initial conditions amplify, making simulation the only practical way to study this sensitivity.

This paper compares experimental and theoretical models of pendulum motion across amplitudes, using experimental data and numerical simulations. The analysis evaluates

the small-angle, nonlinear drag-free, and damped models, and concludes with the exploration of chaotic behavior in the double pendulum.

METHODS

Section 1: Analytically Modelling a Simple Pendulum

1.1 Derivation of the Equations of Motion

To establish a mathematical foundation for modelling a pendulum's motion, Newtonian mechanics is utilized to derive governing equations of motion.

Figure 1.1: Force Diagram for Drag-Free Model [19]

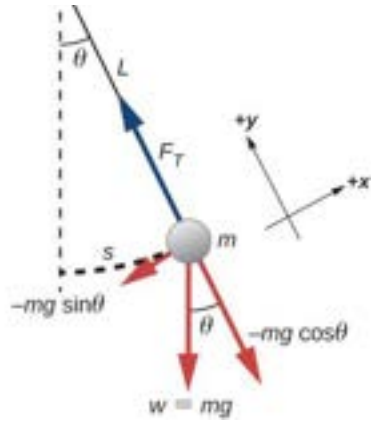

A simple pendulum has the following setup: an assumed point mass *m*, suspended by a massless, rigid rod or string of length *l*, oscillating in a vertical plane under the influence of gravity. The angle *θ* defines the angular displacement from the equilibrium (vertical) position. The restoring force responsible for motion is the component of gravitational force acting tangent to the arc expressed by $F = -mg\sin\theta$. Accordingly, this gives rise to a torque $\tau = -mgl\sin\theta$, where the negative sign indicates opposition to displacement. Considering Newton's second law for rotational motion ($\tau = I\ddot{\theta}$), with $I = ml^2$, the nonlinear differential equation governing the motion derived is:

$$\ddot{\theta} + \frac{g}{l}\sin\theta = 0 \qquad (1)$$

This is a second order, nonlinear ODE that cannot be solved analytically using elementary functions due to the presence of the sine term [20].

The derivation above makes several crucial assumptions including a massless, rigid pendulum rod/string, the bob acting as a point mass, and most importantly, that there is no energy loss due to air resistance or any form of friction at the pivot or internally. This results in an idealized, drag-free model that serves as the foundation for more complex analytical and numerical models. For small angular displacements, though, this equation can be simplified using the small-angle approximation, which is discussed further in the next section.

1.2 Small-Angle Approximation

To simplify the analytically unsolvable nonlinear ODE derived above, a small-angle approximation is widely applied to attain a solution. This is defined as $\sin\theta \approx \theta$, generally valid for $|\theta| \lesssim 0.2\ radians\ (\approx 11^o)$.

This leads to the simplification of the governing nonlinear equation:

$$\ddot{\theta} + \frac{g}{l}\theta = 0 \qquad (2)$$

This is a second-order linear differential equation that describes simple harmonic motion. The general solution is:

$$\theta(t) = \theta_o \cos\left(\sqrt{\frac{g}{l}}t + \emptyset\right) \qquad (3)$$

where θ_o is the initial angular displacement and $\emptyset$ is the phase constant. The period of oscillation under this approximation is:

$$T = 2\pi\sqrt{\frac{l}{g}} \qquad (4)$$

It is important to note that this expression is independent of amplitude, proving its isochronism. This property of a pendulum's motion is what Galileo observed experimentally and used as the conceptual basis for early pendulum clocks, though only strictly valid for small angular displacements [2].

1.3 Extending Beyond the Small-Angle Approximation

Although, as the value of θ rises, the approximation $\sin\theta \approx \theta$ becomes increasingly inaccurate. The Taylor expansion of $\sin\theta$ illustrates this deviation:

$$\sin\theta = \theta - \frac{\theta^3}{6} + \frac{\theta^5}{120} - \ldots$$

The error from truncating at the linear term grows rapidly with the value of the angle. At $\theta = 0.4\ rad\ (\approx 23^o)$, for example, the error exceeds 1% [20]. This point marks a significant error between the estimated and true value of $\sin\theta$. Thus, for

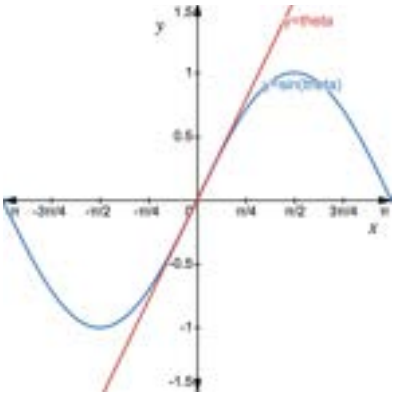

Figure 1.3: Graph comparing sin(θ) and (θ) over a small domain [21]

such large angular displacements, a full nonlinear treatment is necessary. The figure on the right compares $\sin\theta$ (blue line) and θ (red line).

The exact period of a nonlinear pendulum with maximum angular displacement θ_o is given by:

$$T = 4\sqrt{\frac{l}{g}}\int_0^{\pi/2} \frac{1}{\sqrt{1-k^2\sin^2\emptyset}}d\emptyset \qquad (5)$$

where $k = \sin\frac{\theta_o}{2}$, and the integral is the complete elliptic integral of the first kind, denoted *K(k)* [22]

This result is found from energy conservation and advanced techniques in nonlinear differential equations The period increases with amplitude and ultimately diverges as $\theta_o \to \pi$, as it takes an infinite amount of time for the pendulum to reach a vertical upright position from rest.

1.4 Approximations for Moderate and Large Initial Angles of Release

Between the simple linear approximation and the full elliptic solution, several intermediate approximate formulae exist that can closely predict the period for angles larger than those that can be considered as eligible for small-angle approximation. These can be valuable tools since they do this without needing numerical integration through simulation. Two main regimes are considered in this paper:

Not-so-large angle approximation:

For angles less than approximately $\pi/2$, Lima [23] proposes an effective empirical formula that estimates the period using the expression:

$$T \approx -T_o \cdot \frac{\ln(a)}{1-a} \qquad (6),\ where\ a = \cos\left(\frac{\theta_o}{2}\right)$$

Here, T_o is the period in the small-angle limit defined by $2\pi\sqrt{\frac{l}{g}}$, and is the initial (and maximum) angular displacement. This expression yields reasonably accurate estimates for angles below $\pi/2$ and is particularly useful without the availability of numerical tools. However, the error rises monotonically with amplitude and becomes acceptable near π radians.

Very large-angle approximation:

For amplitudes approaching π radians, Cromer's logarithmic formula asymptotically approximates the exact period [24]:

$$T \approx \frac{2}{\pi} T_o \cdot \ln\left(\frac{4}{a}\right) \qquad (7) \quad , \quad where\ a = \cos\left(\frac{\theta_o}{2}\right)$$

This formula diverges logarithmically as $\theta_o \to \pi$, correctly modeling the infinite-period behavior at the vertical upright position. However, it performs poorly at lower amplitudes, where it significantly overestimates the period of oscillation.

Together, these formulae allow for quick approximation across a wide range of angle and serve as useful tools for analysis when high accuracy computational solutions are not feasible. While that is not the case for this paper, it is important to consider them as bridging the significant gap between idealized small-angle theory and complex numerical or elliptic-integra-based solutions.

Section 2. Numerically Modeling a Simple Pendulum

2.1 Analytical Failure in Studying Pendulums

While analytical approaches are often favored for their precision and simplicity, they instantly become insufficient when modeling the true behaviour of pendulum systems beyond ideal approximations and conditions. As displayed in Section 1, the governing equation of the nonlinear pendulum is unsolvable in closed form with only the period derivable using elliptic integrals. If the inclusion of realistic elements is considered (eg. friction or air resistance), the resulting equations become non-integrable using elementary functions. Quadratic damping, for example, introduces velocity-dependent terms that complicate separation of variables that further amplifies this difficulty.

Moreover, when studying multi-body systems such as the double pendulum, analytical methods become impossible. The resulting equations are coupled, nonlinear, and sensitive to initial conditions – a representation of chaotic behaviour. There exists no general solution

analytically to these systems, even under simplifying assumptions. Thus, numerical integration is the only viable route to investigate their dynamics in depth.

2.2 Numerical Solvers and their implementation

Since the pendulum's nonlinear ODE generally has no simple closed-form solution, it is integrated numerically using time-stepping methods explained in Overview of Solving Methods. The initial angle and velocity are inputted and new values at each time set Δt are incrementally computed. In each step the solver uses the current state to estimate the derivates from the defined ODE and update the state to the next time. This numerical approach measures the system's state variables at set time intervals, approximating the continuous motion step-by-step [16].

In general, a variety of numerical algorithms are used to solve ordinary differential equations (ODEs). Four important methods discussed include Euler's Method, Classical Runge-Kutta (RK4), RK45 (Dormand-Price) and DOP853 (Dormand–Prince 8(5,3)). These methods trade of accuracy, speed, and stability.

To start with, Euler's Method is the fastest per step due to just one evaluation but is the least accurate and stable. Its first-order error means the result drifts rapidly unless the step size is extremely minimal [25]. RK4 requires more computation per step but yields much better accuracy for a given step size and is still explicit, so it remains stable in most general situation. RK45 and DOP853 are more refined in the way that they have adaptive stepping, which usually yields higher efficiency. They do this by automatically enlarging the step in smooth regions and shrink it in steep regions, controlling the error. RK45 typically needs fewer total steps than Euler or RK4 for the same tolerance, while DOP853, being 8^{th}-order, can achievably extremely low error but at the cost of many function evaluations. Notably, the SciPy documentation recommends using DOP853 when very high precision is required, such as in chaotic systems like the double pendulum [26]. In summary, one often starts with RK45 as a versatile, middle-ground solver, uses Euler only for quick rough estimates and turns to DOP853 when modelling with high accuracy is crucial.

For regular nonlinear pendulum simulations, RK45 is employed as a reliably and computationally efficient default which has sufficient accuracy to detail the motion of the system. On the other hand, for the chaotic double pendulum, DOP853 is selected due to its enhanced accuracy and lower global error propagation.

2.3 Modeling the Nonlinear Drag-free Pendulum

As outlined earlier, the nonlinear, drag-free pendulum is solved by the exact governing equation:

$$\ddot{\theta} + \frac{g}{l}\sin\theta = 0 \qquad (8)$$

The assumptions for this particular simulation entailed assuming those of a simple pendulum, along with the absence of resistive forces in the form of pivotal and internal friction or air resistance. This assumes complete energy conservation in the motion of the pendulum itself.

Numerical integration is carried out using RK45 for a set number of oscillations with varying initial angles of release, yielding high-resolution time series data for $\theta(t)$ and $\omega(t)$, allowing for the determination of time period. Here, since there is no energy loss, this period remains constant. This value is compared with experimental results from both analytical and numerical methods, along with a lab-based result. While this system is still quite idealized, it provides a critical baseline for understanding more complex behaviour when damping and coupling are introduced.

2.4 Modeling the Damped Nonlinear Pendulum

To model the damped nonlinear pendulum, it is essential to first establish the governing equations that define the motion of the system in this case. The figure below depicts the forces acting on the pendulum, with the restoring force $mg\sin\theta$ and force of drag F_d, acting opposite to the tangential velocity v.

For this paper, the sole resistive force of quadratic drag is assumed– force of drag depending on the factor of linear velocity squared. With this,

Figure 2.4: Force Diagram for Damped Model [27]

$$mL\frac{d^2\theta}{dt^2} = = -mg\sin\theta - \left(\frac{1}{2}C_d\rho A v^2 \times sign(v)\right) \qquad (9)$$

Here,

C_d is the coefficient of drag – approximated to be around 0.5 for spheres [28].

ρ is the air density, which varies with pressure and temperature – assumed to be around 1.204 kgm^{-3} at 20°C and standard pressure [29].

A is the cross-sectional area of the sphere

v is the tangential velocity

$$v = L \times \omega = L\frac{d\theta}{dt} \qquad (10)$$

Substituting $v = L\frac{d\theta}{dt}$ to simplify,

$$mL\frac{d^2\theta}{dt^2} = = -mg\sin\theta - \left(\frac{1}{2}C_d\rho AL^2\left(\frac{d\theta}{dt}\right)^2 \times sign\left(\frac{d\theta}{dt}\right)\right) \qquad (11)$$

$$mL\frac{d^2\theta}{dt^2} + mg\sin\theta + \left(\frac{1}{2}C_d\rho AL^2\left(\frac{d\theta}{dt}\right)^2 \times sign\left(\frac{d\theta}{dt}\right)\right) = 0 \qquad (12)$$

Dividing this equation by '*mL*':

$$\frac{d^2\theta}{dt^2} + \frac{g}{l}\sin\theta + \left(\frac{C_d\rho AL}{2m}\left(\frac{d\theta}{dt}\right)^2 \times sign\left(\frac{d\theta}{dt}\right)\right) = 0 \qquad (13)$$

Since the coefficient of drag, length of the rigid massless rod/string, mass of the bob, air density and the cross-sectional area of the sphere can all be considered to be constant:

Let $\frac{C_d\rho AL}{2m} = \kappa$

Hence,

$$\frac{d^2\theta}{dt^2} + \frac{g}{l}\sin\theta + \kappa\left(\frac{d\theta}{dt}\right)^2 \times sign\left(\frac{d\theta}{dt}\right)) = 0 \qquad (14)$$

which can be represented as:

$$\ddot{\theta} + \frac{g}{l}\sin\theta + \kappa(\dot{\theta})^2 \times sign(\dot{\theta}) = 0 \qquad (15)$$

Simulations were run using RK45, although with tighter error tolerances than in the undamped case to account for the nonlinear damping term and time period decay. The time period evolution would show amplitude decay and period elongation, characteristics of realistic oscillatory motion. These results will be discussed in detail in the experimental results section.

2.5 Modeling the Double Pendulum

The double pendulum system generally consists of two assumedly point masses connected by two assumedly massless rods, both allowed to swing freely in a vertical plane as depicted in the figure below. Unlike the simple pendulum, the system requires two generalized coordinates: $\theta_1(t)$ and $\theta_2(t)$, representing the angular displacement of each mass from the vertical with respect to time.

The complexity of the double pendulum system makes Lagrangian mechanics the preferred framework for deriving its equations of motion. Newtonian mechanics – revolving around forces in action – would require calculating the tensions and constraint forces in both rods independently and resolving them in multiple dimensions. This leads to a cumbersome, lengthy and a less direct derivation.

Lagrangian mechanics, by contrast, allows one to think in terms of energies and generalized coordinate constraints. It inherently accounts for constraint forces and produces a set of compact, coupled equations without requiring a breakdown into individual force components which Newtonian mechanics makes compulsory. This is particularly beneficial in systems with rotational symmetry or non-Cartesian constraints, such as the double pendulum.

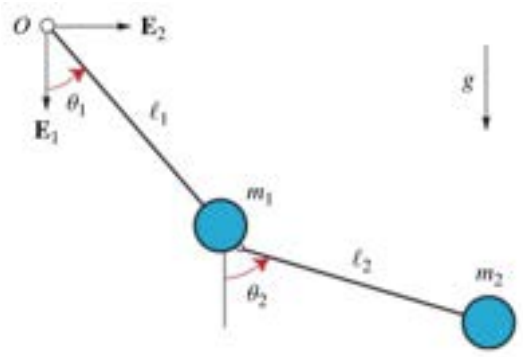

Figure 2.5 Constraint Diagram for Double pendulum
[30]

The Lagrangian (L) serves as the foundation for the Lagrangian approach to mechanics. It is defined as the difference in the total kinetic energy (T) and total potential energy (V) in the system:

$$L = T - V \qquad (16)$$

For the double pendulum, with the plane, coordinates and variables defined as in the figure above,

$$T = \frac{1}{2} m_1 l_1^2 \dot{\theta}_1^2 + \frac{1}{2} m_2 \left(l_1^2 \dot{\theta}_1^2 + l_2^2 \dot{\theta}_2^2 + 2 l_1 l_2 \dot{\theta}_1 \dot{\theta}_2 \cos(\theta_1 - \theta_2) \right) \qquad (17)$$

$$V = -m_1 g l_1 \cos\theta_1 - m_2\, g (l_1 \cos\theta_1 + l_2 \cos\theta_2) \qquad (18)$$

After defining the total kinetic and potential energy in the system, using Lagrange's equations is the next step to derive the equations of motion. These equations are second-order differential equations that describe the motion of a mechanical system [31].

For the double pendulum, there are two generalized coordinates present: θ_1 and θ_2. Euler-Lagrange's equations are applied here to derive equations of motion that look at the change in state of these coordinates with respect to time.

Euler-Lagrange's equations are a fundamental tool in Lagrangian mechanics, and they take the following form:

$$\frac{d}{dt}\left(\frac{\partial L}{\partial \dot{q}_i}\right) - \frac{\partial L}{\partial q_i} = 0 \qquad (19)$$

where *L* is the Lagrangian in terms of generalized coordinates (q_i) and their derivatives with respect to time ($\dot{q}_i$).

Using the expressions for energies involved in the system and the corresponding Euler-Lagrange's equations, the equations of motion are derived for both θ_1 and θ_2:

$$(m_1 + m_2)l_1\ddot{\theta}_1 + m_2 l_2 \ddot{\theta}_2 \cos(\theta_1 - \theta_2) + m_2 l_2 \dot{\theta}_2^2 \sin(\theta_1 - \theta_2) + (m_1 + m_2)g \sin\theta_1 = 0 \qquad (20)$$

$$m_2 l_2 \ddot{\theta}_2 + m_2 l_1 \ddot{\theta}_1 \cos(\theta_1 - \theta_2) - m_2 l_1 \dot{\theta}_1^2 \sin(\theta_1 - \theta_2) + m_2 g \sin\theta_2 = 0 \qquad (21)$$

The full derivation is presented in Appendix A.

After defining these equations of motion, numerical integration is to be performed using the DOP853 solver. This choice is motivated by the need for high-order accuracy (8th Order) to minimize local truncation error. Also, adaptive time-stepping can be done with this to handle the rapid changes in motion associated with the chaotic nature of double pendulums. RK4 and RK45 may diverge in chaotic regimes while the DOP853 is quite reliable to remain stable in these cases.

Plugging initial values for the values for coordinates (q_i) and their derivatives with respect to time ($\dot{q}_i$) and integrating for a set number of oscillations results in a motion configuration highly sensitive to these initial values – a sign of chaotic systems. Plots and further analysis of this behaviour are presented in the Experimental Results section

RESULTS

3.1 Experimental Method

To form a definitive conclusion regarding the effectiveness of different pendulum models at simulating its expected motion, a physical experiment is necessary to conduct to serve as a point for comparison. The setup for the rigid simple-pendulum involves a string with length *L* (measured by a meter stick) and a metal bob – with radius *r* and mass *m* (measured by a meter stick and digital weighing balance respectively) – attached to a low-friction pivot. A digital video camera records the motion of the pendulum for all the initial angles of release at roughly 30 frames/s ($\Delta t \approx 0.03s$) . The LoggerPro software (v. 3.16.2) is used to digitize the bob's position and compute the angular displacement and angular velocity at each timestep. A marked point on the pendulum bob – the center – is used for this computation. At a chosen trajectory, though, the possibility of a rapidly moving bob 'blurring' between pixels makes certain fine details of the path less accurate [32]. In practice, the measured amplitude decayed steadily with time due to air drag and small pivot friction, as expected for a real pendulum [33]. Due to the cumbersome means of data collection, only the experimental data for two angles of release is measured - 10° and 90°. These angles of release are chosen to prove failure of the small-angle approximated model beyond 10°, which has been confirmed theoretically. The 90° release is also shown to measure the significant deviation in the models as well as predict the drag-induced model's accuracy in that case.

A sample of the LoggerPro-derived data is shown below for $\theta_o = 10°$, mapping angular displacement and angular velocity at discrete timestamps. Full datasets are imported into Python for subsequent comparisons error analyses with the simulated models.

[*Table 3.1: Sample LoggerPro output for* $\theta_o = 10°$]

t (s)	x (m)	y (m)	v_x (m/s)	v_y (m/s)	w (rad/s)	theta (rad)
0	0.050824	0.0050009	0	0	0	0.0980802
0.033333	0.045527	0.0034234	0.1907080	0.0279006	0.2961730	0.0750532
0.066667	0.039062	0.0029794	0.2198273	0.0189993	0.0568162	0.0761261
0.1	0.030897	0.0023789	0.2498452	0.015837	0.109380	0.0768443

0.133333	0.021971	0.0018014	0.2691109	0.0099687	0.5468579	0.0818083
0.166667	0.012858	0.0018338	0.2822513	0.0070245	2.5326227	0.1416598
0.2	-0.002839	0.0013666	0.2839983	0.0041078	37.920172	0.4486334
0.233333	0.006386	0.0012055	0.2750978	0.0070625	6.7831845	0.1865678

3.2 Comparison between Theoretical Models

Before comparing to experimental data, it is insightful to gauge how the three theoretical models simulated behave under identical initial conditions. These include:

- The small angle approximated (linearized) model
- The full nonlinear model without damping
- The full nonlinear with quadratic air drag

Simulations were conducted for each model under five standard release angles (10°, 30°, 45°, 60°, 90°), holding physical constants and integration parameters identical. These constants include the length of the string L, the acceleration due to gravity g, the mass m and radius r of the bob. The initial angular velocity was also kept constant at 0 rad/s for all simulations.

The plots obtained are presented below:

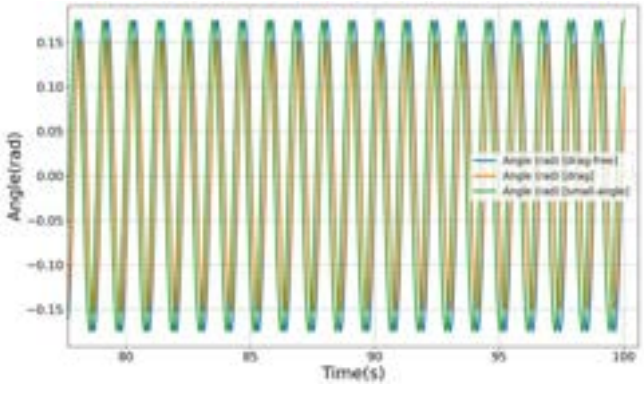

Figure 3.2.1a: θ against t for all models at 10°, *generated from custom Python Simulation*

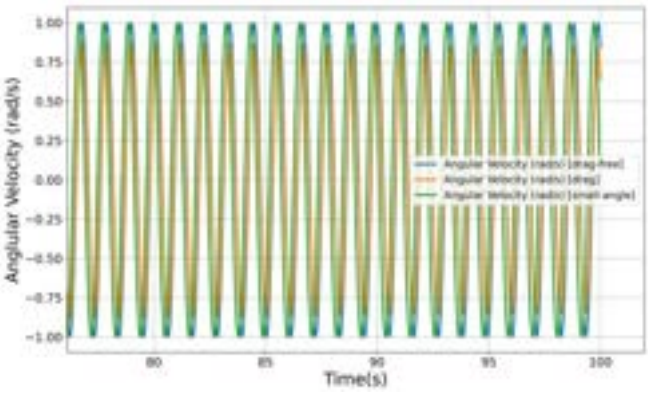

Figure 3.2.1b: w against t for all models at 10°, *generated from custom Python Simulation*

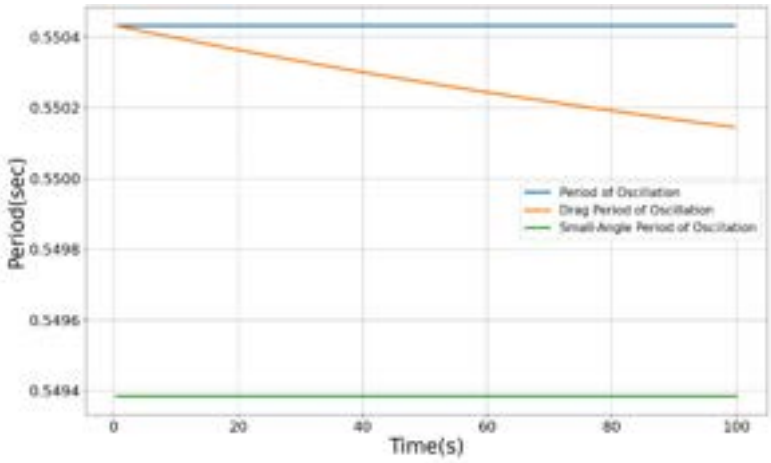

Figure 3.2.1c: Period Evolution for all models at 10°, *generated from custom Python Simulation*

Figure 3.2.2a: θ against t for all models at 30°, *generated from custom Python Simulation*

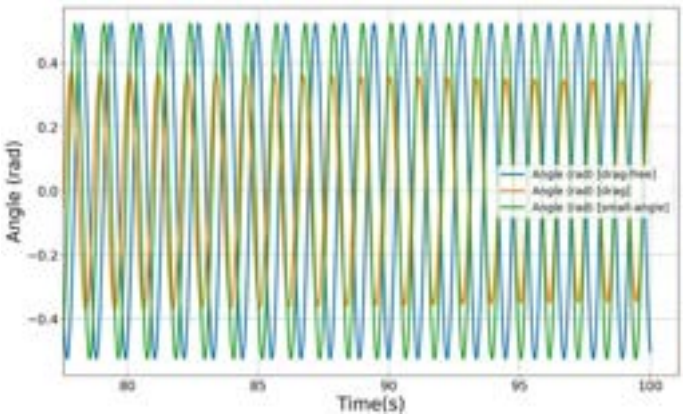

Figure 3.2.2b: ω against t for all models at 30°, *generated from custom Python Simulation*

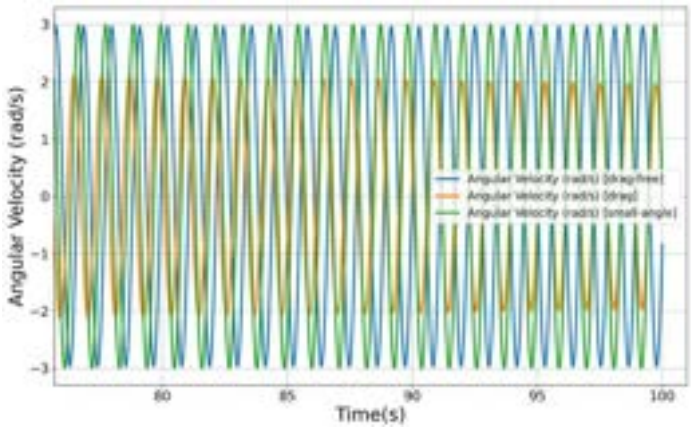

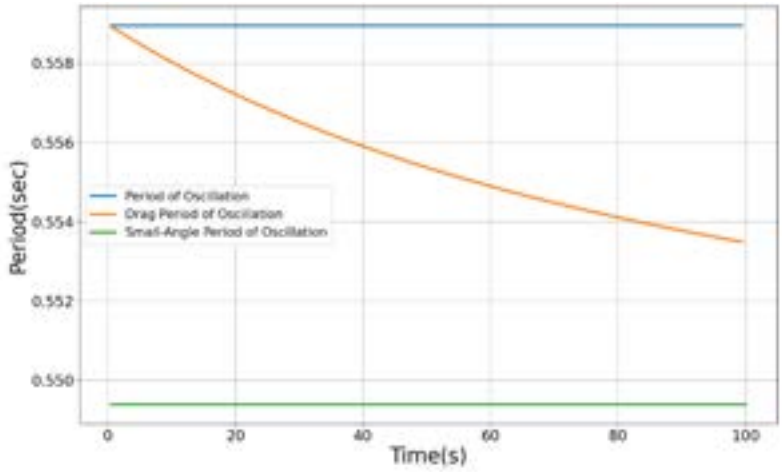

Figure 3.2.2c: Period Evolution for all models at 30°, *generated from custom Python Simulation*

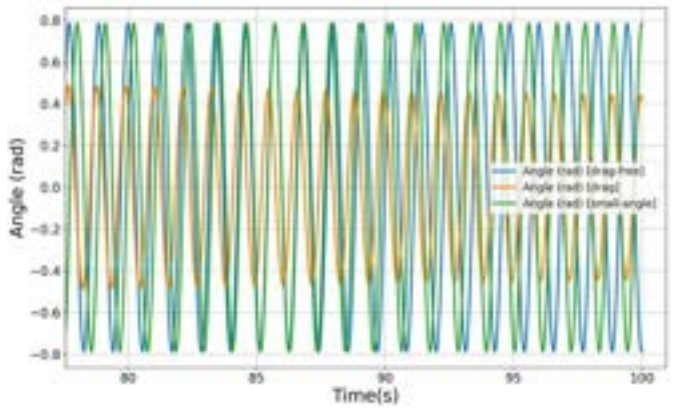

Figure 3.2.3a: θ against t for all models at 45°, *generated from custom Python Simulation*

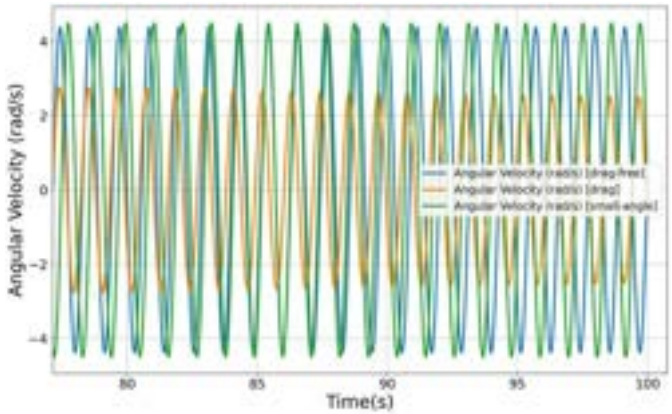

Figure 3.2.3b: ω against t for all models at 45°, *generated from custom Python Simulation*

Figure 3.2.3c: Period Evolution for all models at 45°, *generated from custom Python Simulation*

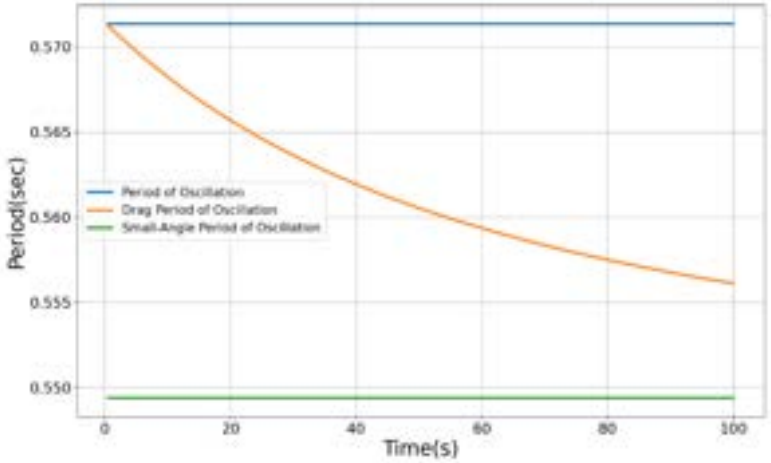

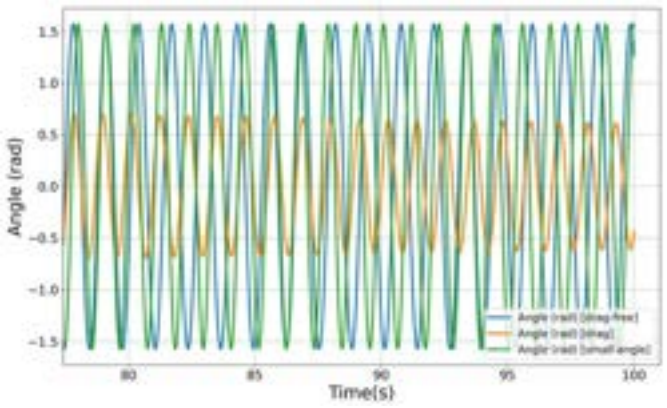

Figure 3.2.4a: θ against t for all models at 60°, *generated from custom Python Simulation*

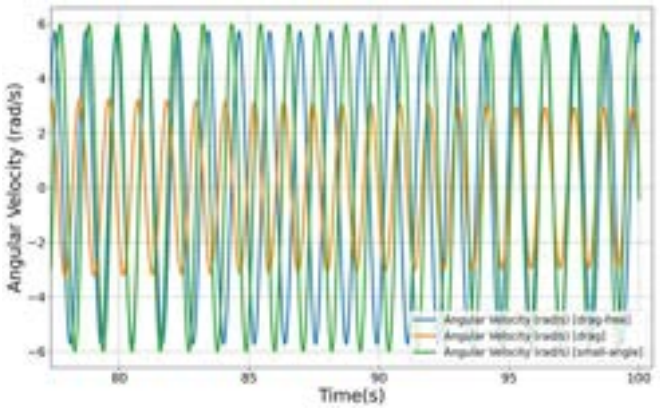

Figure 3.2.4b: ω against t for all models at 60°, *generated from custom Python Simulation*

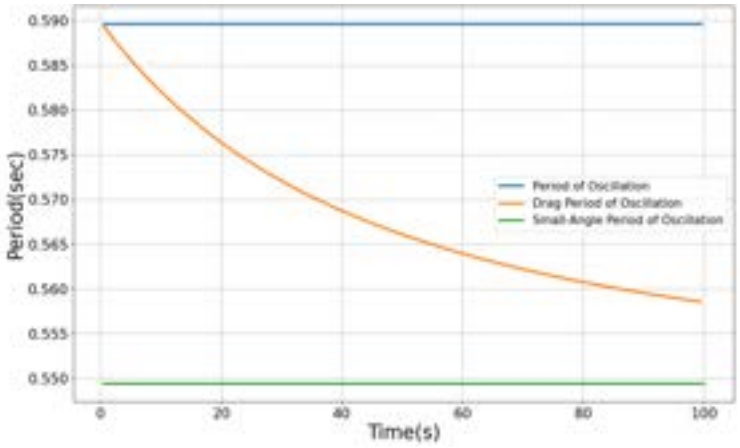

Figure 3.2.4c: Period Evolution for all models at 60°, *generated from custom Python Simulation*

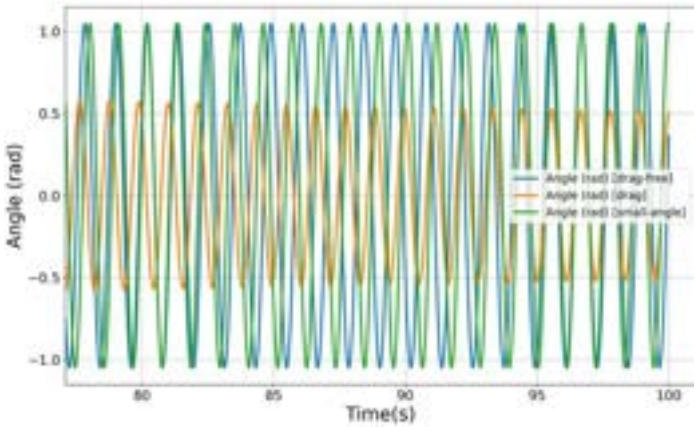

Figure 3.2.5a: θ against t for all models at 90°, *generated from custom Python Simulation*

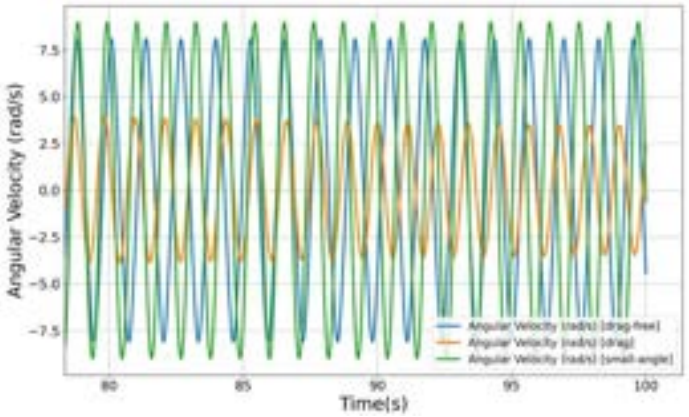

Figure 3.2.5b: ω against t for all models at 90°, *generated from custom Python Simulation*

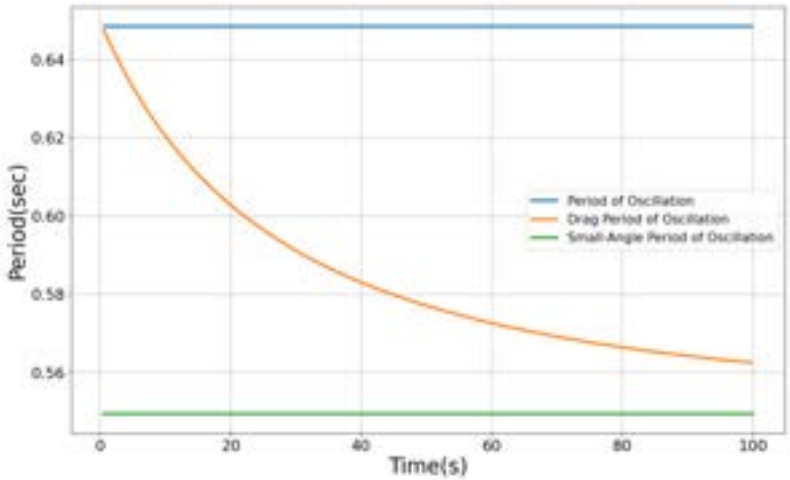

Figure 3.2.5c: Period Evolution for all models at 90°, *generated from custom Python Simulation*

Note that for all graphs: (blue = drag-free model) (orange = drag model) (green = small-angle model)

For extremely low displacement (10°), all three models exhibit nearly identical displacement and velocity profiles. The small-angle approximation aligns closely with the nonlinear models, with only a minor phase offset. Quadratic drag introduces a slight amplitude decay of ~20% by the final cycle. Period evolution curves confirm the similarity: both the small-angle and drag-free models remain constant, differing by just 0.001 s, while the damped model shows only a subtle decay of 0.0004 s.

At 30°, small nonlinear effects emerge. The small-angle approximation now shows a perceptible phase lead, nearly half an oscillation ahead over 100 s. Amplitude decay in the drag model reaches ~30%. Period differences grow an order of magnitude, with the small-angle model ~0.01 s shorter than the drag-free model, while damping shortens the period by 0.006 s.

At 45°, divergence becomes significant. The small-angle model completes an entire oscillation more than the drag-free model, with period error rising to 0.023 s. The drag-free and damped models remain aligned in phase, but the damped case shows 40–45% amplitude and velocity reduction. Its final period is ~0.015 s shorter than the drag-free version.

By 60°, the limitations of the small-angle approximation are undeniable, with more than two extra oscillations compared to the nonlinear models. Its period underestimates by ~0.04 s, nearly double the error at 45°. Drag effects dominate: amplitude and velocity decay exceed 50%, and the damped model's final period is shortened by ~0.03s.

At the extreme case of 90°, the small-angle model leads by over 2.5 oscillations, overestimating peak velocity by ~1 rad/s. Amplitude decay in the drag model reaches ~55%, while its period shortens by ~0.03 s relative to drag-free. Notably, period errors grow consistently with angle: from 0.001 s at 10° to nearly 0.1 s at 90°.

Overall, results show that while the small-angle approximation is valid at low displacements, it rapidly fails at larger angles due to cumulative phase error and period underestimation. The drag-free nonlinear model accurately predicts period but neglects amplitude decay. The drag-induced model best reflects experimental damping trends, with growing significance at higher energies.

3.3 Deviation from Experimental Data

To quantify the accuracy of each theoretical model simulated in approximating real pendulum motion, the angular displacement and angular velocity generated for the full duration of simulation were directly compared to the LoggerPro experimental output (See Figure 3.1) for the angles of release tested. Since the time base for the simulation is not identical to that of the experimental measurements (at 30 FPS or in intervals of 0.03 seconds), the simulated data is to be interpolated to match the experimental timestamps. For release points not tested experimentally, the drag-induced model is considered as a point of reference due to its inherently increased accuracy. Thus, it can serve as an approximate basepoint.

The deviation at each time point is the absolute value of difference between the simulation and experiment given by:

$$\Delta\theta(t) = \left|\theta_{sim}(t) - \theta_{exp}(t)\right|$$

$$\Delta w(t) = \left|w_{sim}(t) - w_{exp}(t)\right|$$

(i) For extremely low initial displacement - 10°

Figures 3.3.1a and 3.3.1b below plot the results for $\theta_o = 10°$ for the three models. In this case, the models yield consistently low deviation values, with the small-angle approximated and drag-free models performing nearly identically. The angular displacement deviation difference and the angular velocity deviation difference between models is negligible. It is important to note that absolute error is high for the angular velocity for some cases, but this is due to experimental error, not in the model. Thus, it can be inferred that for this release angle, all 3 models are adept at accurately approximating real pendulum motion.

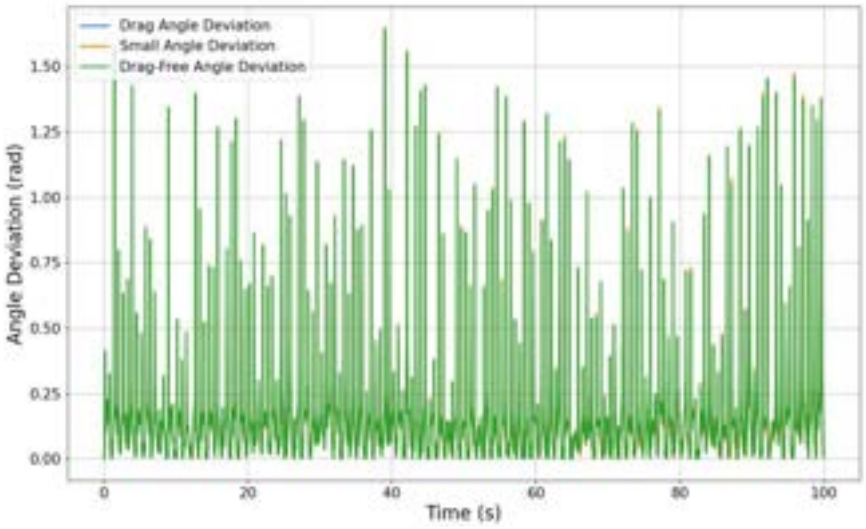

Figure 3.3.1a: $\Delta\theta$ against t for all models at 10°

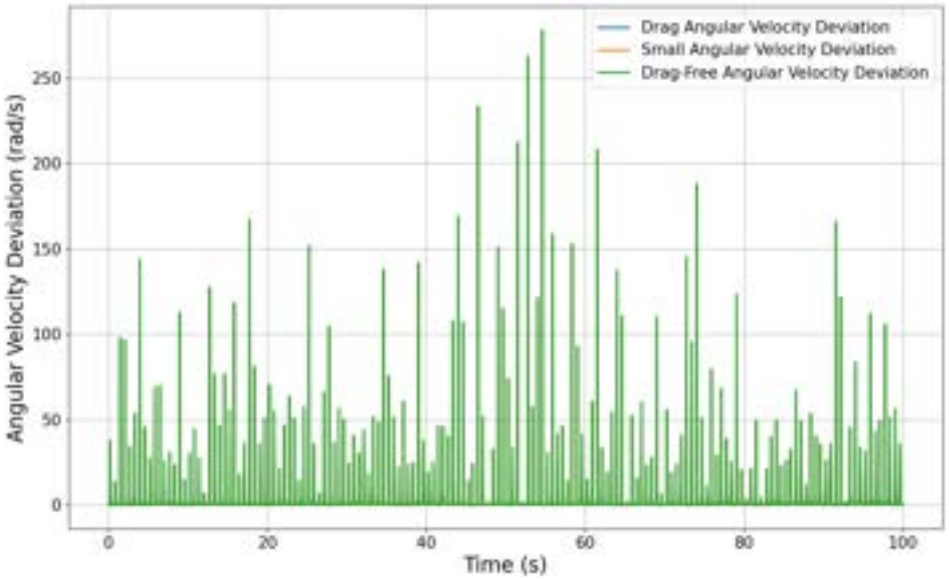

(ii) For low initial displacement - 30°

For the 30° case, the small-angle model begins to drift as compared to the drag-free model which performs better to model this motion in the first few oscillation cycles. Peak angular deviation is at 1 rad and peak angular velocity error goes over 5 rad/s. The drag-free model still generally works for this initial angle of release, with a much smaller deviation of angle (0.5 rad) and angular velocity (2 rad/s). However, as observed in both Figures 3.3.2a and 3.3.2b, the nonlinear undamped model fails to model the eventual shrinking oscillation time

period due to its assumed constant period for the entire simulation period. Surprisingly, the small-angle approximated model has a much lower deviation toward the latter half of the simulation period at in both angle (0.25 rad) and angular velocity (< 2 rad/s).

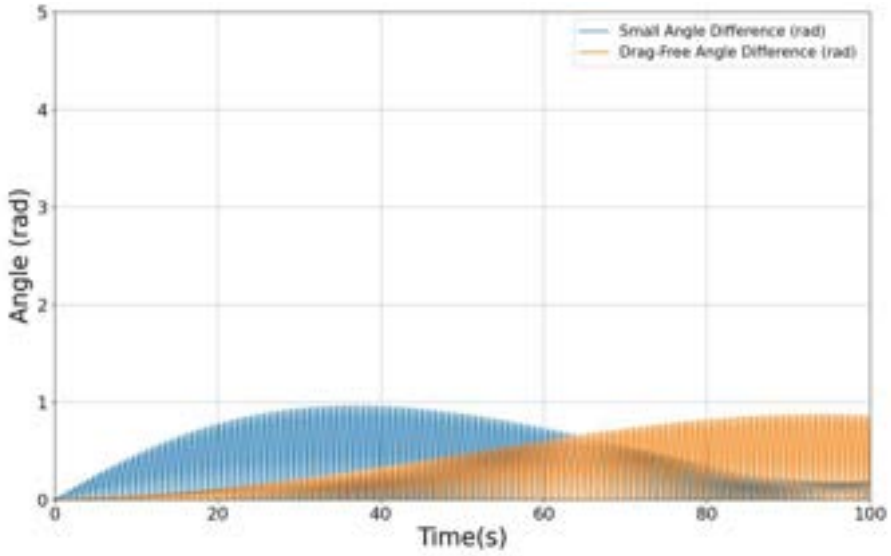

Figure 3.3.2a: $\Delta\theta$ against t for all models at 30°

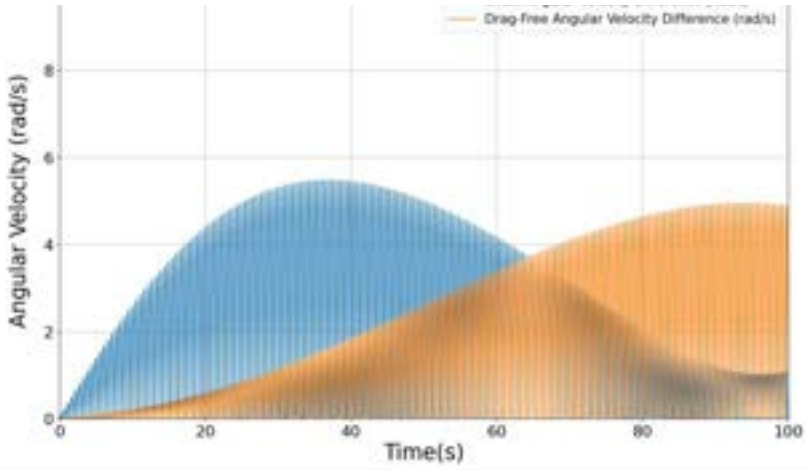

Figure 3.3.2b: Δw against t for all models at 30°, *generated from custom Python Simulation*

(iii) For moderate initial displacement - 45°

At this angle of release, the significant error in both phase and peak state values for the small-angle approximated and drag-free become particularly noticeable over the full oscillation time. For the small-angle approximated model over the simulation period, angular error reaches close to 1.5 rad, while maximum error in angular velocity climbs over 8 rad/s. Additionally, the drag-free model also begins to exhibit significant error in the angular

deviation toward the last few oscillation cycles, around 1.5 rad, and in angular velocity – close to 8 rad/s. It also starts to show signs of deviating in phase. One thing to note here is the consistent trend of deviation appearing in the drag-free model only after multiple oscillations due to its failure in modelling decay. Again, the small-angle approximated model can be used as a close estimate for the last few cycles of oscillations as seen in its lower deviation in that frame of time.

Figure 3.3.3a: $\Delta\theta$ against t for all models at 45°, *generated from custom Python Simulation*

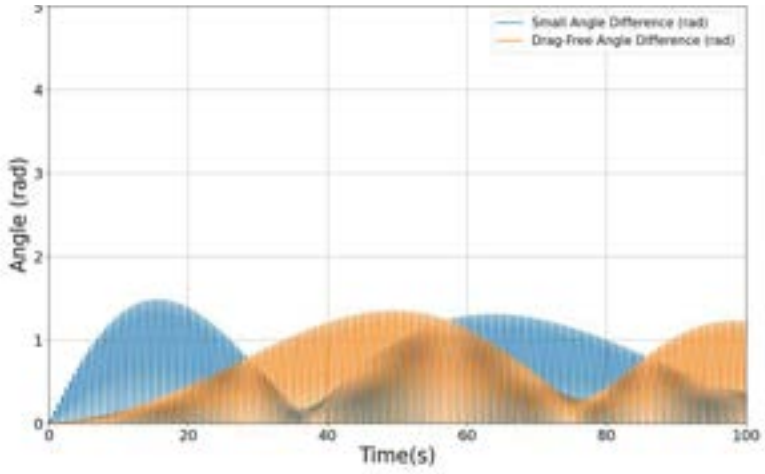

Figure 3.3.3b: Δw against t for all models at 45°, *generated from custom Python Simulation*

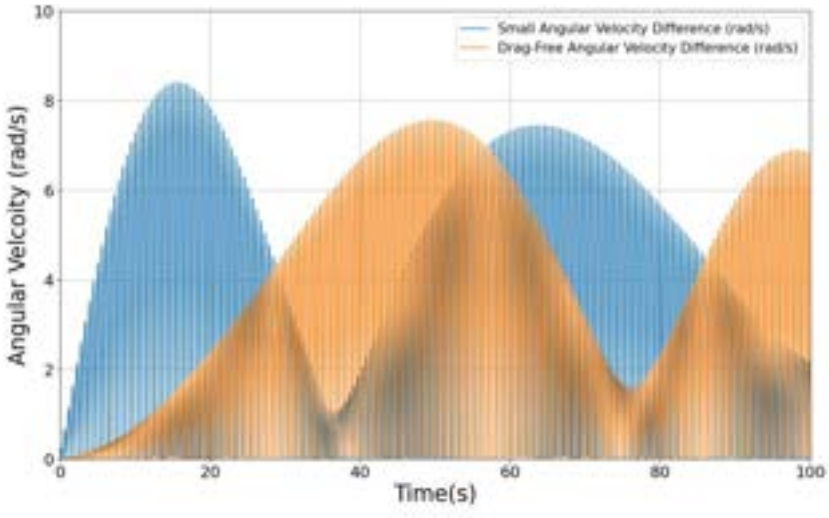

(iv) For high initial displacement - 60°

In this case, the errors are amplified further. The small-angle approximation becomes of no use while even the nonlinear drag-free solution has significant error in modeling the behavior.

Here, in fact, even the later oscillations where the small-angle approximated model had better results previously, it has great error. The peak angular displacement and velocity deviation in the models comes close to 2 rad and 11 rad/s respectively. This deviation is in both the models.

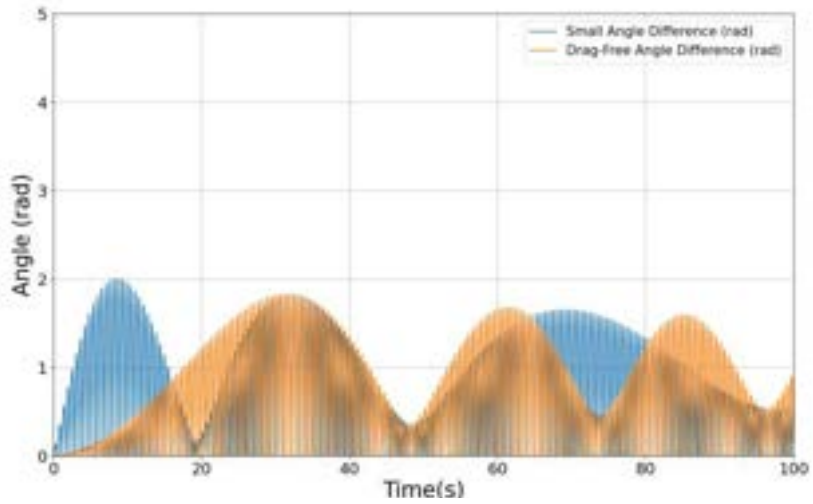

Figure 3.3.4a: $\Delta\theta$ against t for all models at 60°, *generated from custom Python Simulation*

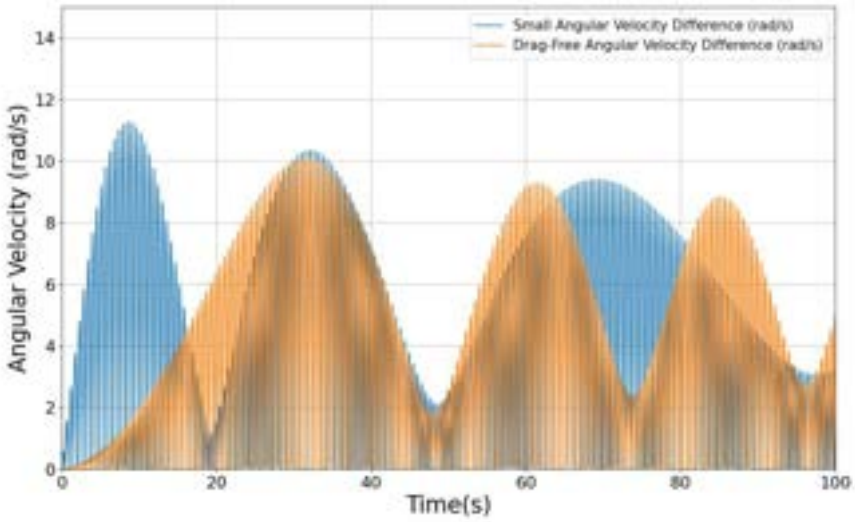

Figure 3.3.4b: Δw against t for all models at 60°, *generated from custom Python Simulation*

(v) For extremely high initial displacement - 90°

The most interesting case in comparing the models lies in the comparing the results at the unstable angle of release of 90°. This is why results were compared over a full 100-second

simulation to effectively accuracy at the most nonlinear form. Over the complete simulation period, the small-angle model completes over 2.5 extra oscillations than the actual pendulum due to a great underestimation in period. While error in the small-angle and drag-free model plateaus due to the damping, deviation exceeds 15 and 13 rad/s respectively. The drag model displays half of that error and more consistently has lower deviation than the other models. The damped model tracks amplitude decay reasonably well as its difference in angular displacement to the experimental data remains the least at 1.7 rad at maximum, as compared to the maximum of 3 rad observed in the other models. It remains the best performing model of the bunch in accurately mapping experimental real data.

Figure 3.3.5a: $\Delta\theta$ against t for all models at 90°

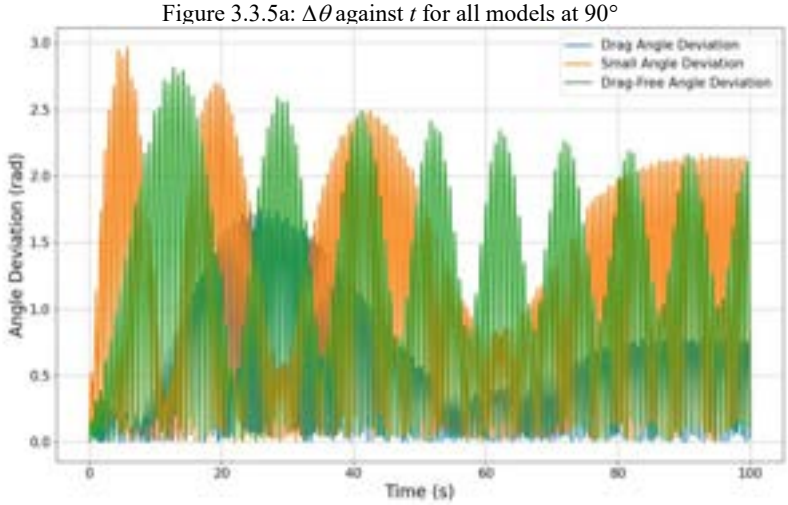

Figure 3.3.5b: Δw against t for all models at 90°

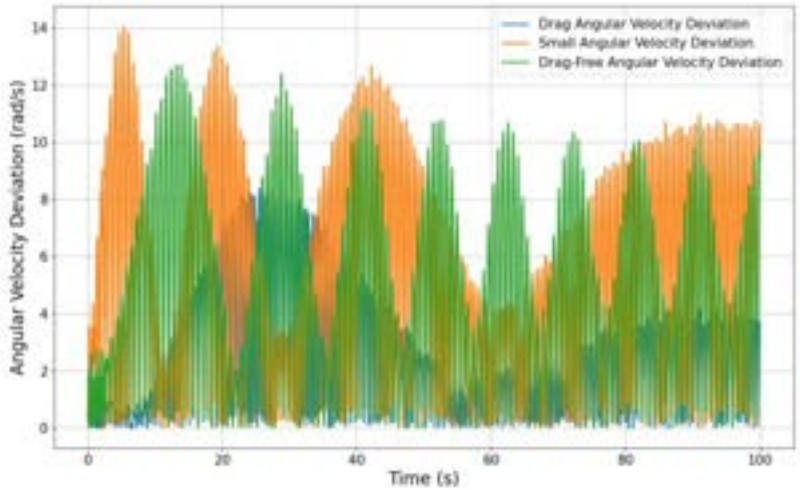

3.4 Time Period Analysis

3.4.1 Methodology of Period Extraction

Time periods for each model are determined based on oscillation extracted from w(t) or θ(t) plots for both experimental and simulated data. Due to the recording of multiple oscillations of data, two references for comparison are made for ease and effectiveness for the angles of release - 10º and 90º. Namely, the points are the average of the first three oscillations and the average of the last three oscillations in the 100 second time frame.

For simulations, high-resolution time arrays from numerical solvers used were analyzed to detect events where the state value crossed 0. Periods were calculated by measuring the time between alternate zeroes in the state vs time plot. The first three and last three values are averaged for each of the models to quantify change in period over time as well as establish a good comparison point for the experimental results. As mentioned, the data is here interpolated to match the time intervals of the experimental data.

For the experimental data recorded via LoggerPro, angular velocity versus time was extracted for each initial displacements at a sampling rate of 30 FPS or in 0.03s intervals. The period was determined numerically by importing the tabular data to Python which extracts period that can be averaged similarly to the simulated data. Overall, methodology allows for the reporting of experimental periods up to 4 decimal places to have consistency with the simulated data.

3.4.2 Comparative Data and Bar Chart

Table 3.4.2: Comparison of time periods for experimental and Simulated Data.

Initial Angle (°)	***Oscillation***	T_{exp} (s)	T_{small} (s)	$T_{drag\text{-}free}$ (s)	T_{drag} (s)
10	Early-cycle	0.6127	0.5494	0.5504	0.5504
	Late-cycle	0.5882	0.5494	0.5504	0.5502
30	Early-cycle	-/-	0.5494	0.5589	0.5587
	Late-cycle	-/-	0.5494	0.5589	0.5536
45	Early-cycle	-/-	0.5494	0.5713	0.5704

	Late-cycle	-/-	0.5494	0.5713	0.5563
60	Early-cycle	-/-	0.5494	0.5896	0.5871
	Late-cycle	-/-	0.5494	0.5896	0.5588
90	Early-cycle	0.7167	0.5494	0.6485	0.6873
	Late-cycle	0.5400	0.5494	0.6485	0.5629

Figure 3.4.1: Bar chart of percent error in period for first vs final oscillation across all models and angles.

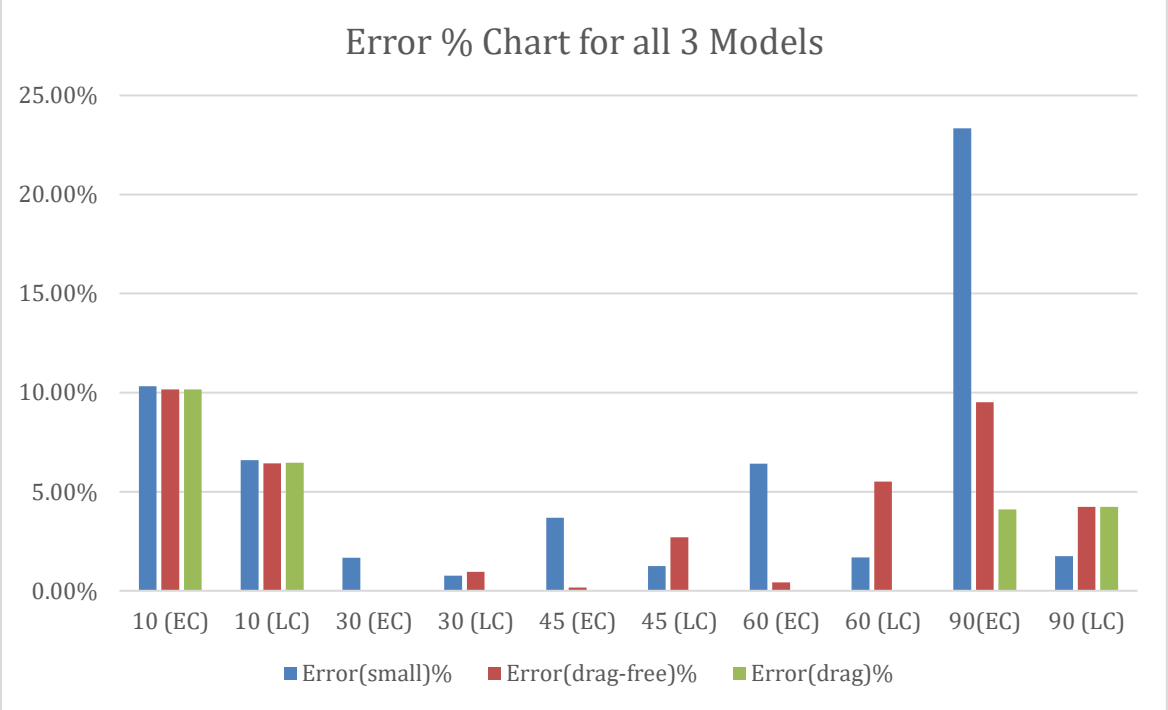

3.4.3 Observed Trends and Implications

Looking at Table 3.4.1 and Figure 3.4.1, there are some prevalent trends in the data that appear when comparing the simulation and experiment.

Firstly, all models converge at 10° and diverge with higher angles. This is due to the relevance of the small-angle approximation – since it lies in the valid range – and the insignificant damping due to limited initial energy level that allow for nearly constant periods. This reduces the error for the models that predict constant periodic motion – drag-free and small-angle approximated. Although, as the initial displacement increases, the models

diverge. Secondly, when looking at the small-angle approximation model usefulness, it rapidly loses accuracy beyond 30° where it fails to account for nonlinear behavior. Moreover, the drag-free model retains good short-term prediction but overestimates long-term periods as suggested by Figure 3.4.1 which shows its great error in predicting the average period for the last few oscillation cycles. One interesting trend is that at 90°, damping effects level off slightly, as compared to the rapid increase over the angles less than 90°. This suggests an asymptotic trend in period decay, as discussed in Section 3.3.

These results reinforce that nonlinear and damping effects dominate at larger amplitudes, and that model choice is angle dependent. Fine-tuning damping coefficients based on air density, material choice, and drag-coefficient based on geometry may further improve high-angle model fidelity.

3.5 Model Suitability Summary

The comparative results presented in Sections 3.2 through 3.4 reveal crucial insights into the range of validity and applicability of each theoretical model. Based on state vs time behavior, period evolution, and experimental deviation, the following model choices emerge as most appropriate across each amplitude:

(i) **For extremely low initial displacement - 10°:** All three-models perform equally well. The small-angle approximation yields nearly identical results to the nonlinear models that must be solved numerically, so the analytical approach of the small-angle approximation takes precedent here. Due to its simplicity, the **small-angle approximated** model is preferred.

(ii) **For low initial displacement - 30°:** For this case, however, the small-angle approximated model begins to break down and show visible underestimation in period as well as phase mismatching. The drag-free nonlinear model, along with the damped model, matches closely with the experiment in early cycles. Due to the computational burden and additional information required about the setup for the drag model, the **drag-free** model is preferred in cases where either short-term oscillations are studied or alternate factors such as air density and drag coefficient cannot be approximated or found. Thus, it is generally preferred.

(iii) **For moderate initial displacement - 45°:** At this point the small-angle model is out of the picture, particularly with its large error in phase and total number of oscillations in the time period. The drag-free model and damped model follow the same trend as the 30° but the error in amplitude measure and time period is now significant for the last few oscillation cycles for the drag-free model. However, it does still accurately map initial oscillations. Thus, the **drag-free** model is preferred for early cycles while the **drag-induced** model is the answer if longer time periods are modelled or if higher accuracy is necessary. **Both** models here could be used.

(iv) **For high initial displacement - 60°:** Now, looking at only the drag-free and drag-induced model, there is a similar pattern as the 45° amplitude, but there is now error that is evident even in the early oscillations of the drag-free model. It predicts period shape and state trends but is insufficient to model the pendulum accurately. Hence, due to its enhanced accuracy in mapping amplitude and period decay, the **drag-induced** model is the clear option for this model.

(v) **For extremely high initial displacement - 90°:** Between the nonlinear models, the drag-induced model is preferred at this high energy level. The drag-free model starts with accurate motion but quickly breaks down as rapid damping takes precedent. Thus, to model this the drag-induced model is suitable. It is important to note, though, that there is some deviation in the model. This underscores the need for careful coefficient calibration here to obtain accurate values for other variables such as air density, radius of bob, drag-coefficient and more involved in the drag model's calculations.

3.6 Double Pendulum Simulation Results

To demonstrate the transition from predictable oscillatory behaviour to chaotic dynamics, a double pendulum model was included. Even with the addition of just one extra degree of freedom, the system shifts from regular motion to highly sensitive and unpredictable trajectories, emphasising the broader relevance of nonlinear dynamics beyond the simple pendulum. This system was modelled using a Lagrangian mechanics formulation and integrated via

the high-precision DOP853 solving method, with parameters chosen to mirror those of the simple pendulum for meaningful comparison.

This was run for 100 seconds using 100,000 seconds (Δt = 0.001 s), allowing fine-grained resolution to track the system's rapid dynamic changes. The parameters used were:

- Arm Length: $L1 = L2 = 0.3m$
- Masses: $m1 = m2 = 0.01kg$
- Initial Angular Displacements: $\theta_o 1 = \theta_o 2 = 30°$
- Initial Angular Velocities: $w1 = w2 = 0$

The simulation output included a trace animation of the lower bob (tip of the second pendulum), with the pendulum traced across its full trajectory. The result is a densely plotted, curving path showing the space traversed over the full period of simulation. Figure 3.6.1 represents this at one timestamp in the animation.

Figure 3.6.1: Double Pendulum Simulated Animation with Trace Plot

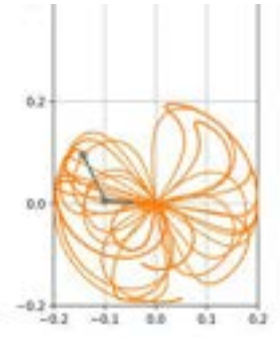

One thing to note here is that despite the minimal initial energy input – at a low initial angle of release – the trace reveals chaotic motion beginning after a short initial phase of close to regular oscillation. As energy exchanges between the two arms amplify, the lower bob follows a highly sensitive, unpredictable, and chaotic path characterized by loops and crossings. This simulation visually demonstrates the exponential divergence of trajectories and the impossibility of predicting behavior without high-resolution integration as conducted.

The use of equal arm lengths and masses simplify the theoretical model but still produce rich dynamical behavior due to the uncanny nonlinear coupling between the bobs. The

animation confirms that even small deviations in initial conditions set the motion in a dramatically altered trajectory.

This simulation highlights the extent of testing numerical methods, exploring deterministic chaos and modeling it. While analytical solutions are not possible in these cases, high-resolution solvers such as DOP853 provide a practical tool for revealing some pattern to the chaotic motion.

CONCLUSION

This study evaluates the effectiveness and degree of accuracy of various pendulum models in capturing real-world motion, progressing from simple idealizations to complex nonlinear systems. Through thorough simulations and experimental comparisons, the paper has reaffirmed the importance of the pendulum as well as numerical tools in engineering. Importantly, the investigation reveals the experimental limits of the small-angle approximation in adequately describing pendulum motion over long intervals and with moderate and large amplitudes.

The nonlinear drag-free model improves considerable upon this by consistently aligning in phase and amplitude behavior, especially at intermediate angles. However, its inability to capture damping renders it inadequate for long-term behavior studies. The full nonlinear model, with quadratically dependent air resistance, while computationally more intensive and sensitive to parameter selection, emerges as the most accurate to experimental values. Period decay, as an important defining characteristic of real-pendulum systems, is effectively mapped in this model. However, the accuracy of the drag term is limited by the choice of damping coefficient, which was difficult to calibrate precisely. Small variations in bob radius, air density, or the assumed drag coefficient can significantly alter the predicted energy loss, leading to mismatch with experiment. This highlights a key limitation of the current modelling: while quadratic drag captures the overall trend of amplitude decay, achieving quantitative agreement requires careful experimental determination of damping parameters, which was beyond the scope of this study.

Beyond the simple pendulum, the double pendulum simulations underscores the transition from deterministic dynamics to chaotic motion. This pushes the line of numerical simulation, with a high-resolution solver necessary to render its full motion. Even with relatively low initial

energies, the system displays sensitivity to parameters inputted. A simulation output with an animation of this system traces out this unpredictable motion.

Altogether, this study demonstrates the necessity of pendulum model selection based on system energy and highlights the importance and usefulness of accurate numerical simulation as an indispensable toolkit for capturing real-world motion. From metrology to structural dynamics and chaos theory, the pendulum is not only historically significant but deeply relevant to modern science and engineering with tools available in this time.

Appendix A

This appendix provides a full derivation of the equations of motion for a planar double pendulum using Lagrangian mechanics.

M1: $x_1 = l_1 \sin\theta_1\ ,\ y_1 = -l_1 \cos\theta_1$

M2: $x_2 = l_1 \sin\theta_1 + l_1 \sin\theta_2\ ,\ y_2 = -l_1 \cos\theta_1 - l_2 \cos\theta_2$

The corresponding velocities are:

M1: $\dot{x}_1 = \dot{\theta}_1 l_1 \cos\theta_1\ ,\ \dot{y}_1 = \dot{\theta}_1 l_1 \sin\theta_1$

M2: $\dot{x}_2 = \dot{\theta}_1 l_1 \cos\theta_1 + \dot{\theta}_2 l_2 \cos\theta_2\ ,\ \dot{y}_2 = \dot{\theta}_1 l_1 \sin\theta_1 + \dot{\theta}_2 l_2 \sin\theta_2$

Hence, the total kinetic energy is:

$$\frac{1}{2} m_1 (\dot{x_1}^2 + \dot{y_1}^2) + \frac{1}{2} m_2 (\dot{x_2}^2 + \dot{y_2}^2)$$

Simplifying in terms of existing variables:

$$T = \frac{1}{2} m_1 l_1^2 \dot{\theta}_1^2 + \frac{1}{2} m_2 \left(l_1^2 \dot{\theta}_1^2 + l_2^2 \dot{\theta}_2^2 + 2 l_1 l_2 \dot{\theta}_1 \dot{\theta}_2 \cos(\theta_1 - \theta_2) \right)$$

The total potential energy (*V*) is:

$$V = -m_1 g l_1 \cos\theta_1 - m_2\, g (l_1 \cos\theta_1 + l_2 \cos\theta_2)$$

Plugging these values into the Lagrangian Function

$$L = T - V$$

$$L = \frac{1}{2} m_1 l_1 \dot{\theta}_1^2 + \frac{1}{2} m_2 \left(l_1^2 \dot{\theta}_1^2 + l_2^2 \dot{\theta}_2^2 + 2 l_1 l_2 \dot{\theta}_1 \dot{\theta}_2 \cos(\theta_1 - \theta_2) \right) + m_1 g l_1 \cos\theta_1 + m_2\, g (l_1 \cos\theta_1 + l_2 \cos\theta_2)$$

Substituting *L* into the Euler-Lagrange Equation for *i* = 1,2,

$$\frac{d}{dt}\left(\frac{\partial L}{\partial \dot{q}_i}\right) - \frac{\partial L}{\partial q_i} = 0$$

This leads to the Final Equations of Motion:

$$(m_1 + m_2) l_1 \ddot{\theta}_1 + m_2 l_2 \ddot{\theta}_2 \cos(\theta_1 - \theta_2) + m_2 l_2 \dot{\theta}_2^2 \sin(\theta_1 - \theta_2) + (m_1 + m_2) g \sin\theta_1 = 0$$

$$m_2 l_2 \ddot{\theta}_2 + m_2 l_1 \ddot{\theta}_1 \cos(\theta_1 - \theta_2) - m_2 l_1 \dot{\theta}_1^2 \sin(\theta_1 - \theta_2) + m_2 g \sin\theta_2 = 0$$

Bibliography

[1] J. M. Norman, “Huygens Invents the Pendulum Clock, Increasing Accuracy Sixty Fold,” History of Information, 1656. [Online]. Available: https://www.historyofinformation.com/detail.php?id=3068. [Accessed: Jun. 12, 2025].

[2] M. Hafez, *Dynamics of Structures: The Pendulum Paradigm*. Springer, 2015.

[3] M. Levis, “Why Is the Pendulum So Popular?,” *Quanser Blog*, Sept. 16, 2019. [Online]. Available: https://www.quanser.com/blog/control-systems/why-is-the-pendulum-so-popular/. [Accessed: Jul. 7, 2025].

[4] D. A. Russell, “The Simple Pendulum,” *Penn State University*, 2011. [Online]. Available: https://acs.psu.edu/drussell/Demos/Pendulum/Pendula.html. [Accessed: Jul. 9, 2025].

[5] “Circular Error in a Pendulum,” *AbbeyClock*, [Online]. Available: https://www.abbeyclock.com/pendulumerror.html. [Accessed: Jul. 7, 2025].

[6] R. D. Knight et al., *University Physics*, 2nd ed., OpenStax, 2017. [Online]. Available: https://openstax.org/books/university-physics-volume-1. [Accessed: Jul. 11, 2025].

[7] W. McAllister, “RLC Natural Response – Intuition,” *SpinningNumbers*, June 2, 2020. [Online]. Available: https://www.spinningnumbers.org/a/rlc-natural-response-intuition.html. [Accessed: Jul. 11, 2025].

[8] H. Broer, M. Seri, and F. Takens, *Oscillations: Swings and Vibrations from a Mathematical Viewpoint*, Cambridge University Press, 2024.

[9] Altair, “Building for Safety and Security in Skyscrapers,” *Altair Engineering Blog*. [Online]. Available: https://www.altair.com/blog/articles/Building-for-Safety-and-Security-in-Skyscrapers. [Accessed: Jul. 13, 2025].

[10] D. Zhou et al., “Seismometers, Seismographs, Seismograms – What’s the Difference?” *U.S. Geological Survey, 2020*. [Online]. Available: https://www.usgs.gov/faqs/seismometers-seismographs-seismograms-whats-difference-how-do-they-work. [Accessed: Jul. 11, 2025].

[11] NASA, “Space Math: Measuring Gravity with a Pendulum,” *NASA Goddard Space Flight Center*, 2003. [Online]. Available: https://spacemath.gsfc.nasa.gov/weekly/10Page39.pdf. [Accessed: Jun. 12, 2025].

[12] J. R. Chasnov, “The Damped, Driven Pendulum,” *Scientific Computing (LibreTexts)*. [Online]. Available: https://math.libretexts.org/... [Accessed: Jun. 18, 2025].

[13] 3D-ScanTech, “Numerical Simulation,” *3D-ScanTech Solutions, 2024*. [Online]. Available: https://www.3d-scantech.com/solution/numerical-simulation/. [Accessed: Jun. 22, 2025].

[14] J. Brownlee, “Analytical vs Numerical Solutions in Machine Learning,” *MachineLearningMastery.com*, Mar. 14, 2018. [Online]. Available:

https://machinelearningmastery.com/analytical-vs-numerical-solutions-in-machine-learning/. [Accessed: Jun. 15, 2025].

[15] APEX Calculus, “Graphical and Numerical Solutions to Differential Equations,” *Moravian University*. [Online]. Available: https://webwork.moravian.edu/apexcalc/sec_diffeq_graph_numer.html. [Accessed: Jun. 10, 2025].

[16] APMonitor.com, “Dynamic Modeling,” *APMonitor, 2025*. [Online]. Available: https://apmonitor.com/do/index.php/Main/DynamicModeling. [Accessed: Jun. 25, 2025].

[17] L. Davis, “Testing the Simple Pendulum Model,” *Atlantic OER (Nova Scotia CC)*. [Online]. Available: https://pressbooks.atlanticoer-relatlantique.ca/remotegenphys/chapter/testing-the-simple-pendulum-model/. [Accessed: Jun. 19, 2025].

[18] University of California, Santa Barbara, "Pendulum Damped by Air." *Lecture Demonstrations*. [Online]. Available: https://web.physics.ucsb.edu/~lecturedemonstrations/Composer/Pages/40.37.html. [Accessed: Jun. 9, 2025].

[19] T. J. Millikan (ed.), “Figure 1.1: Force Diagram for Drag-Free Model,” *University Physics II — PHY2048, Chapter 15.4*, Pressbooks, UCF. [Online]. Available: https://pressbooks.online.ucf.edu/phy2048tjb/chapter/15-4-pendulums/. [Accessed: Jun. 14, 2025].

[20] E. T. Whittaker and G. N. Watson, *A Course of Modern Analysis*, 4th ed., Cambridge Univ. Press, 1927, p. 157.

[21] StudyWell, “*Figure 1.3: Graph comparing sin(θ) and θ over a small domain*,” *Small Angle Approximations*, StudyWell Trigonometry. [Online]. Available: https://studywell.com/trigonometry/small-angle-approximations/. [Accessed: Jul. 7, 2025].

[22] J. A. Crawford, “Pendulums and Elliptic Integrals,” 2004. [Online]. Available: https://www.jamescrawford.org/pendulum/. [Accessed: Jun. 16, 2025].

[23] R. Lima, “Period of a Non-linear Pendulum at Moderate Angles,” 2006. [Online]. Available: (Original reference). [Accessed: Jun. 21, 2025].

[24] A. Cromer, “Asymptotic Period Formula for Large-Angle Pendulum,” [Online]. Available: (Original reference). [Accessed: Jun. 23, 2025].

[25] Monroe Community College, “Euler’s Method*,” MTH225 Differential Equations*. [Online]. Available: https://math.libretexts.org/Courses/Monroe_Community_College/MTH_225_Differential_Equations/03:_Numerical_Methods/3.01:_Euler%27s_Method. [Accessed: Jun. 11, 2025].

[26] SciPy Documentation, “scipy.integrate.solve_ivp,” *SciPy v1.7.1 Reference Manual*. [Online]. Available: https://docs.scipy.org/doc/scipy/reference/generated/scipy.integrate.solve_ivp.html. [Accessed: Jun. 13, 2025].

[27] Wikimedia Commons contributors, “Figure 2.4: Force Diagram for Damped Model,” *Wikipedia – Pendulum (mechanics)*, Feb. 3, 2024. [Online]. Available: https://en.wikipedia.org/wiki/File:Pendulum.png. [Accessed: Jun. 17, 2025].

[28] B. R. Munson et al., *Fundamentals of Fluid Mechanics*, 8th ed., Wiley, 2017, p. 446.

[29] E. W. Lemmon et al., “Thermophysical Properties of Air and Mixtures of Nitrogen, Argon, and Oxygen,” *Journal of Physical and Chemical Reference Data*, vol. 29, no. 3, pp. 331–385, 2000. doi:10.1063/1.1285884.

[30] J. Murad, “Figure 2.5: Constraint Diagram for Double Pendulum,” in *The Double Pendulum: Equations of Motion & Lagrangian Mechanics*, Engineered Mind, 2022. [Online]. Available: https://www.engineered-mind.com/engineering/double-pendulum-1/. [Accessed: Jul. 7, 2025].

[31] J. Murad, “The Double Pendulum: Equations of Motion & Lagrangian Mechanics,” *Engineered Mind,* 2022. [Online]. Available: https://www.engineered-mind.com